CARBON 47 (2009) 2904–2913

available at www.sciencedirect.com

ScienceDirect

journal homepage: www.elsevier.com/locate/carbon

Detailed structural models for activated carbons from molecular simulation

J.C. Palmer[a,*], J.K. Brennan[b], M.M. Hurley[b], A. Balboa[c], K.E. Gubbins[a]

[a]Department of Chemical and Biomolecular Engineering, North Carolina State University, Raleigh, NC 27695, USA
[b]US Army Research Laboratory, Weapons and Materials Research Directorate, Aberdeen Proving Ground, MD 21005, USA
[c]US Army Edgewood Chemical Biological Center, Research and Technology Directorate, Aberdeen Proving Ground-Edgewood Area, MD 21010, USA

ARTICLE INFO

Article history:
Received 16 April 2009
Accepted 15 June 2009
Available online 21 June 2009

ABSTRACT

A detailed atomistic model of Calgon Co.'s bituminous coal-based activated carbon (BPL) was developed using an adaptation of the Hybrid Reverse Monte Carlo method. The resulting model was a highly heterogeneous carbon structure that had features consistent with experimental X-ray diffraction measurements. The microstructure of the model was characterized and Grand Canonical Monte Carlo simulations were used to examine the adsorptive properties of the model. These findings were compared with experimental measurements taken on samples of the real material. The results showed that the model provides a realistic description of the BPL's microstructure and accurately predicts adsorptive behavior over a wide range of state conditions.

1. Introduction

Activated carbons are among the most widely used industrial materials. Due to their low cost of production and high adsorption capacity, they have found use in a number applications such as gas and electrolyte storage, gas and fluid purification, and as catalysts and catalyst supports [1–4]. Activated carbons are typically synthesized from organic carbonaceous precursors such as woods, coconut shells and coals. By judicious choice of the precursor materials and processing conditions, they can be synthesized with a wide range of features characterized by pore size distribution (PSD), specific surface area (SSA) and chemical composition. As a result, a considerable amount of effort has been expended into characterizing activated carbons in order to understand how specific structural and chemical features influence their performance (e.g. [5–7]). Despite these efforts, their highly amorphous nature has limited the ability of traditional structural characterization techniques, such as X-ray diffraction (XRD), to fully resolve the detailed microstructure of these materials. As a result, a fundamental understanding of how their structural features give rise to their adsorptive properties remains elusive and thus the ability to develop activated carbons with optimal properties for specific applications has not yet been achieved.

Molecular simulation methods have been widely used to study the adsorptive properties of porous materials (e.g. [8–11]). The primary limitation in applying these methods to study activated carbons has been the lack of realistic structural models. The most frequently used approach has been to use highly simplified geometric models such as infinite slit or cylindrical shaped pores to model the porous structures in activated carbons [12,13]. While these models account for variations in pore size, they fail to adequately capture sources of heterogeneity such as pore connectivity and irregular pore morphologies. More detailed structural models have been developed by so-called *reconstruction* methods that generate atomistic models to match key experimental measurements,

* *Corresponding author:* Fax: +1 919 513 2470.
E-mail addresses: jcpalmer@ncsu.edu, cord.palmer@gmail.com (J.C. Palmer).
0008-6223/$ - see front matter
doi:10.1016/j.carbon.2009.06.037

such as the pore size distribution or radial distribution function (RDF) [14,15]. Structural models produced by reconstruction methods incorporate pore connectivity and irregular pore shapes, but without additional constraints these methods do not provide an accurate description of the carbon microstructure and usually produce models that contain unrealistic structural features such as highly strained three- and four-member carbon rings.

Recent advances in the understanding of covalent bonding in solids from experimental studies and first-principles quantum mechanical calculations have allowed for the development of reactive intermolecular potentials that accurately describe the energetics and geometry of bonding in hydrocarbon systems [16,17]. Opletal et al. were the first to use one of these potentials in conjunction with a reconstruction method. The resulting simulation technique, known as Hybrid Reverse Monte Carlo (HRMC), was used to generate a model for an amorphous carbon that both reproduced the targeted structural function and had a physically reasonable microstructure [18]. This method was developed further by Jain et al. and was used to generate structural models for three microporous carbons derived from saccharose [19]. Their models reproduced the experimental RDFs with a high degree of accuracy and had a very low occurrence of highly strained bonded structures. Subsequently, the HRMC method has also been used successfully to develop models for activated carbon fiber [20], a wood-derived ultra-microporous activated carbon and a non-activated carbon derived from crystalline TiC [21].

Our goal is to develop a structural model for Calgon's bituminous coal-based carbon, BPL. BPL is a widely used industrial adsorbent that has shown promise in environmental applications, particularly as an adsorbent for toxic and odorous industrial chemicals [6,22–26]. There have been many approaches taken to model BPL including those based on classical thermodynamic theories [27,28] and molecular simulation and statistical mechanics [29–31]. Segarra and Glandt [29] and Liu and Monson [30,31] have both proposed platelet models for BPL, in which the carbon framework of BPL is modeled as a collection of randomly positioned and oriented graphite platelets, consisting of either one or two featureless, planar graphene sheets. This approach has been very successful in reproducing experimental adsorption data over a wide range of state conditions for a number of adsorbates, including methane, ethane and their mixtures, and water. While the platelet models go well beyond the slit-pore approximation by introducing sources of heterogeneity such as pore connectivity and variable pore morphologies, they do not provide the atomistic-level detail needed to allow for local structural deviations from that of graphite, such as curvature of the basal graphite sheets, deviations in the carbon bonding chemistry or a realistic description of the polydispersity of graphene fragment sizes found in BPL. As a result, the ability of these models to accurately predict the structural features of BPL and their impact on the adsorption properties is limited.

The structural model proposed here is a fully atomistic model for BPL that was constructed using the HRMC method. The model addresses the shortcomings of the slit-pore and platelet models by including key sources of heterogeneity such as variability in the pore size, pore interconnectivity, irregular pore geometries and deviations in the local microstructure from that of crystalline graphene, while accurately reproducing the experimental carbon density profile of the real material. We examine the structural features of the proposed model in considerable detail and calculate geometric properties such as the carbon ring size distribution, bond angle distributions and ring connectivity [32] and illustrate that these features are very different from those found in crystalline graphite. In addition, the geometric pore size distribution and surface area are calculated using exact Monte Carlo integration techniques. The adsorptive properties of the model are also examined for several simple fluids and compared directly with experimental measurements.

2. Experimental methods

2.1. X-ray diffraction

BPL (12×30 mesh) granular activated carbon was purchased from Calgon Carbon Co. (lot No. 0325). A powdered sample was prepared by grinding and sieving the BPL to remove particles larger than 45 μm. XRD measurements were taken on the powdered sample using the Advanced Photon Source at Argonne National Laboratory with a Moly Ka source at a wavelength of 0.284812 Å in the 2θ range of 2–68° with a 0.01° step size. Background contributions from the sample holder were subtracted and standard corrections for adsorption and polarization were made. The resulting intensities were normalized using a method based on the principle of the conservation of intensity described in detail by Franklin [33]. After normalization and subtraction of the incoherent contribution, the structure factor, $S(q)$, was obtained. The RDF was then calculated from the structure factor using the MCGOFR method of Soper [34], which uses a reverse Monte Carlo procedure to estimate the RDF such that the presence of spurious oscillations and other truncation errors that result from the finite range of q are minimized.

2.2. Adsorption measurements

Volumetric adsorption measurements were taken on BPL samples using a Quantachrome Autosorb 1C analyzer to measure nitrogen adsorption and desorption isotherms at 77 K. The nitrogen isotherms were used to estimate the differential PSD for BPL using the quenched-solid non-local fluid density functional theory (QSDFT) of Ravikovitch and Neimark [35] implemented in the Quantachrome data reduction and analysis software, ASWin ver. 1.55. While this implementation of non-local density functional theory still assumes a simple slit-pore geometry in calculating the properties of the carbon sample, it treats the solid carbon phase as a quenched component, allowing for a heterogeneous carbon density profile to be incorporated into the slit-pore model. Thus additional sources of heterogeneity in the microstructure that are not explicitly taken into account may be incorporated into the slit-pore model through an effective surface roughness, resulting in improved estimates of the PSD for highly heterogeneous materials such as activated carbons. The linear

region of the nitrogen adsorption isotherm was also used to estimate the SSA of BPL using Brunauer–Emmett–Teller (BET) analysis [36].

3. Theoretical methods

3.1. The Hybrid Reverse Monte Carlo method

The HRMC method is a stochastic simulation technique that is used to efficiently sample configurational phase space based upon an energy functional, U, which describes the potential energy of the system in terms of atomic coordinates, molecular orientations and other configurational degrees-of-freedom, while simultaneously minimizing the mean squared error between the model and experimental RDFs. For simple systems where the bonding structure and energy functional are well known, the global energy minimum corresponds to a thermodynamically stable and unique atomic configuration. However, for more complex systems, such as covalently-bonded solids, energy functionals that can accurately describe correlations between atoms beyond a few angstroms have not been developed. Thus, a biasing function is used to account for long-range correlations in the potential energy, which dictates the micro- and meso-scopic structures. In our simulations, we have used the total residual error cost function, χ^2, which is calculated between the simulated and experimentally measured RDFs, $g(r)$,

$$\chi^2 = \sum_{i=1}^{n} (g_{\mathrm{sim}}(r_i) - g_{\mathrm{exp}}(r_i))^2. \quad (1)$$

The sampling is conducted with the total number of particles, N, and the total volume of the system, V, held constant. In addition, the ratio of a temperature-like parameter, T, and a weighting factor, w, that is related to the total error in the experimental RDF, is also held constant. The Metropolis acceptance probability in the HRMC procedure for transitioning from one configuration to another is a function of both the change in configurational energy and residual error,

$$P^{\mathrm{accept}} = \min[1, \exp(-(\Delta U + w\Delta\chi^2)/T)]. \quad (2)$$

Further details of the HRMC method can be found elsewhere [19,37].

3.2. Generation of the model

The HRMC method was used to generate a structural model for BPL. Along with the RDF, the mean carbon density on the length scale of the simulation cell must also be known to generate an initial starting configuration. This, however, is a nontrivial quantity to determine directly from experiment as the measured density varies considerably between the microscopic and macroscopic length scales. For example, the *apparent density* for BPL, or packed particle density, ranges from 0.4 to 0.5 g/cm^3 depending on the particle size. The *particle density*, as measured by mercury displacement, gives an estimate of the density that includes the void space contribution due to micropores and small mesopores and has been reported to be 0.8 g/cm^3 for BPL. And finally, the *true density*, which excludes void volumes that are large enough to be accessible to helium, is 2.23 g/cm^3, or roughly that of crystalline graphite [24].

Since the HRMC method is best suited for microporous systems, we estimated the carbon density using the approach taken by Nguyen et al. [20], in which the density, ρ_c, is

$$\rho_c \approx \frac{X_C}{\frac{1}{\rho_{He}} + V_{MP}}, \quad (3)$$

where X_c is the weight percent of carbon in BPL, ρ_{He} is the true density as measured by helium displacement and V_{MP} is the micropore volume. This method was chosen because it provides an estimate of the density that includes only the void space of the micropores. The micropore volume was estimated to be 0.44 cm^3/g by integrating over the PSD that was calculated using QSDFT and the value for the true density was taken from Ref. [24]. Since BPL is synthesized from bituminous coal, it contains a number of heteroatoms such as N, O, H, S and Cl. The composition of the BPL may also vary from batch to batch depending on the composition of the coal precursor. We chose X_c such that the micropore volume of our final structure matched our estimate of the micropore volume obtained from the PSD, where the method for calculating the model's micropore volume is discussed in Section 3.4. Therefore using $X_c = 0.935$ and $V_{MP} = 0.44$ cm^3/g in Eq. (3), the carbon density used to construct the model was 1.05 g/cm^3.

Simulations were initiated from a randomly-generated initial configuration of 1420 carbon atoms in a periodic cubic unit cell, 30 Å in length. Beyond 15 Å, oscillations in the experimental RDF were not observed, indicating it did not contain significant structural information. Therefore, the length of the unit cell was chosen so that a RDF cutoff of 15 Å could be used while keeping the minimum image convention [38]. An annealing procedure was also implemented by varying w and T in such a way that their ratio remained constant during the simulation. This was done to ensure that configurational space was adequately sampled during the simulation and that the final structural model would not be heavily influenced by the choice of our initial starting configuration. The HRMC method was used to perform 10^4 blocks of 3.5×10^4 Monte Carlo steps. The ratio w/T and annealing rate were chosen such that the final simulated and experimental RDF were in good agreement and no highly strained small carbon rings structures were observed. To calculate the configurational energy in our simulations and to capture bond breaking and formation, we used the Adaptive Intermolecular Reactive Empirical Bond Order (AIRBEO) potential of Stuart et al. [16].

3.3. Structural characterization

One of the key advantages of building structural models for activated carbons is that their microstructure features can be examined by exact geometric methods. Using the method of Franzblau [39], we identified all of the carbon rings in our model structure assuming minimum and maximum carbon bonding distances of 1.2 Å and 1.8 Å, respectively. Once the individual rings were identified, ring connectivity analysis was performed using the method of Jain and Gubbins [32], which allowed us to identify graphene microcrystals in our model. In defining the graphene microcrystals, we accounted for deviations from an ideal six-member ring crystal structure

and included defects such as five- and seven-member carbon rings and non-planar hexagonal rings. In our calculations, a microcrystal was then defined as any continuous segment containing only five-, six- and seven-member carbon rings.

The total geometric pore size distribution was calculated using the method of Gelb and Gubbins [9], which uses a spherical probe to determine the largest sphere that may be inserted at a given point in the simulation cell without overlapping the carbon structure. The pore width is then defined as the diameter of this largest sphere. We sampled approximately 10^6 points using an evenly spaced grid to discretize the space of the simulation cell. Overlap was defined to occur if the probe sphere came within the Lennard-Jones diameter, 3.36 Å, of the geometric center of a carbon atom. The Connolly surface area of the model structure was calculated using the chord length distribution method described in Ref. [40]. This measure of the surface area is the area that would be obtained if a spherical probe were rolled over the carbon structure. Therefore, any region of the structure accessible to the surface of the probe molecule contributes to the total surface area. For our calculations, we used a sphere of 3.75 Å in diameter, which is the Lennard-Jones diameter of the nitrogen model used in this study.

3.4. Simulated adsorption isotherms

Grand Canonical Monte Carlo (GCMC) simulations [41] were used to calculate simulated adsorption isotherms on our model structure. The adsorbate molecules and carbon atoms were modeled as single-site Lennard-Jones spheres. The adsorbate collision diameters and well-depths, as well as the adsorbate-carbon collision diameters were taken from Nguyen et al. [20]. The adsorbate-carbon well-depths, ε^{sf}, were scaled from the parameters for graphite, ε_G^{sf},

$$\varepsilon^{sf} = \alpha\varepsilon_G^{sf}, \tag{4}$$

by a constant scaling factor, α. The scaling factor is used to correct the adsorbate-carbon parameters originally developed by Steele for interaction of adsorbates with graphitized carbon black [42]. Using quantum mechanical calculations, Klauda et al. have recently shown that the adsorbate-carbon parameters for nitrogen and oxygen interacting with curved carbon surfaces deviate significantly from the original Steele parameters due to the changes in the carbon electron cloud distribution [43]. In practice, the scaling factor is used to account for the changes in the dispersion energy due to surface curvature as well as other sources of heterogeneity not explicitly considered, such as the presence of heteroatoms and unknown systematic sources of error in the measured density profile. A scaling factor of 1.10 was found to give the best fit between the simulated and experimental adsorption isotherms for nitrogen. It is interesting to note that the scaling factor was very close to the scaling factor of 1.134 used by Nguyen et al. for adsorption onto activated carbon fiber [20]. The same scaling factor was then used to scale the well-depths of helium, carbon dioxide and methane. A summary of the parameters used in this study is presented in Table 1. To lessen computational expense, interactions between the adsorbate molecules and the carbon surface were calculated at approximately 5.4×10^6 evenly spaced grid points prior to the start of the simulation. These values were tabulated in a look-up table that was accessed during the simulation runtime, where a linear interpolation scheme was used to obtain the value of the potential energy between grid points. All interactions were truncated after 15 Å. At each state point along the isotherm, the simulations were equilibrated using a minimum of 5×10^6 Monte Carlo steps. Statistics were then collected over a minimum of 10×10^6 additional Monte Carlo steps. Each subsequent simulation was initialized using the final configuration from the previous one.

For nitrogen at 77 K, the bulk phase in equilibrium with the adsorbed nitrogen was assumed to be an ideal gas and the difference between the absolute and excess amounts adsorbed were assumed to be negligible. For carbon dioxide and methane, the relationship between the chemical potential and bulk pressure was calculated using the Lennard-Jones equation of state [44]. The absolute and excess amounts adsorbed, n, were related by,

$$n^{\text{excess}} = n^{\text{absolute}} - V^P\rho^{\text{bulk}}, \tag{5}$$

where V^P is the total pore volume and ρ^{bulk} is the bulk density of the adsorbate under identical state conditions. Following the prescription of Myers and Monson [45], the pore volume was estimated by helium adsorption at 298 K. To save computational cost, the bulk densities were estimated using the Lennard-Jones equation of state.

Differential enthalpies of adsorption, q_d, were calculated from the fluctuations in the number of adsorbate molecules in the simulation cell, N, and the configurational energy, U, during the GCMC simulations,

$$q_d = RT - \frac{\langle UN\rangle - \langle U\rangle\langle N\rangle}{\langle N^2\rangle - \langle N\rangle^2}, \tag{6}$$

where the brackets indicate that the values are ensemble averages [46].

4. Results and discussion

4.1. Details of the microstructure

Using the HRMC method, a model structure for BPL was generated. As illustrated in Fig. 1, the RDF of the model was in very good agreement with the experimental RDF, with an average residual error of 0.01 per data point.

Both RDFs had relatively sharp first and second peaks, corresponding to first and second bonding neighbors, which indicated that there was some degree of local ordering. However, the intensity of subsequent peaks decayed rapidly until no distinguishable ordering was observed beyond approximately 10 Å. There were also no observable features in the range of 3.3–3.5 Å in the RDFs, which would correspond to the interlayer spacing in graphite. This suggested that neither the model nor the BPL sample contained a significant amount of stacked graphene microcrystals.

The average first and second neighbor distances, l_1 and l_2, respectively, were obtained from the experimental RDF by fitting the first two peaks to Gaussian functions. For the model, these distances were computed exactly from the structure. From both RDFs, we also computed the neighbor distribution functions, $n(r)$,

Table 1 – Lennard-Jones parameters used in this study.

Species	Fluid–fluid diameter, σ (Å)	Fluid–fluid well-depth, ε/k_B (K)	Fluid–carbon diameter, σ (Å)	Scaled fluid–carbon well-depth, ε/k_B (K)
Helium	2.557	10.22	2.980	16.50
Nitrogen	3.750	95.20	3.360	67.54
Methane	3.751	148.00	3.576	70.74
Carbon-dioxide	3.648	246.15	3.400	89.44

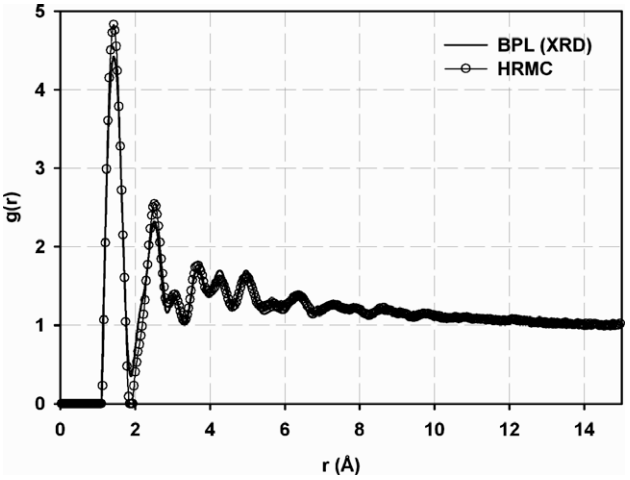

Fig. 1 – Radial distribution functions for BPL (from XRD) and the HRMC-generated model.

$$n(r) = \int_0^{\infty} 4\pi\rho_c r^2 g(r) dr, \quad (7)$$

which gave the average number of carbon atoms in the first and second coordination shells n_1 and n_2, respectively. We also used the model to calculate carbon bond angle, θ, and torsion, or dihedral, angle, ϕ, distributions. These quantities were compared with those calculated from an ideal graphite crystal constructed using lattice parameters that were taken from Ref. [47]. The findings from these calculations are summarized in Table 2.

While the distances for the first and second neighbors were consistent with those of graphite, the first neighbor coordination numbers for both BPL and the model were significantly less. The second neighbor coordination numbers were slightly higher than that of graphite. This was due to the fact that the second neighbors can only occur in the plane of the same graphene sheet in graphite, while for amorphous carbons, second neighbors are not confined to a plane and may occur anywhere in a spherical cutoff radius from the central atom, with or without being bonded to a first neighbor.

In addition to the deviations in the coordination numbers, the large variance in the bond and torsion angles indicated that a wide variety of local bonding and ring structures were present. For the model, the variance in the bond angle encompassed both 108° and 128.57°, which corresponded to the angles in ideal planar five- and seven-member carbon rings, respectively, and indicated that these structures may have been present. There were also torsion angles that significantly deviated from 180°, i.e., planar graphene. Thus, these features illustrated that even at the most local level for the BPL sample and the HRMC model, the structure was highly heterogeneous and deviated significantly from that of crystalline graphite. This was confirmed by examining a snapshot of the final structure, shown in Fig. 2.

To examine the model structure in greater detail and confirm the presence of five- and seven-member rings, we computed the ring statistics for the HRMC model. The model structure contained a significant proportion of five-, six- and seven-member rings as well as non-planar forms of these structures, as was expected from the analysis of the RDF and bond angles. The distribution of ring sizes is presented in Table 2. It is also important to note that there was a complete absence of three- and four-member ring structures. Therefore, the HRMC method was effective in eliminating these highly strained ring structures by incorporating energetic constraints into the reconstructive procedure. We also performed ring connectivity analysis to identify any larger structural features such as graphene microcrystals. While there were a number of graphene microcrystals present in the structure, the average segment consisted of only 18.7 carbon atoms, with a large standard deviation of 9.6 atoms. Several representative graphene microcrystals are illustrated in Fig. 2. As was also observed from the snapshot, the microcrystals were generally highly curved and consisted of mostly five- and six-member carbon rings, with no more than 44 carbon atoms present in the largest microcrystal. The small size of the segments and the fact that only 25% of the total

Table 2 – Bonding characteristics and ring statistics. Where appropriate, values are presented in the form of mean ± standard deviation. Blank cells indicate that the property could not be directly calculated from the available data.

Substance	Neighbor distances, l_1, l_2 (Å)	Coordination #s, n_1, n_2 (atoms)	Bond and torsion angles, θ, ϕ (°)	Ring statistics 5,6,7-member (%)
Graphite	1.42, 2.46	3.0, 6.0	120.0, 180.0	0.0, 100.0, 0.0
BPL	1.44 ± 0.19, 2.49 ± 0.24	2.89, 6.24	–	–
Model	1.45 ± 0.13, 2.53 ± 0.21	2.91, 6.34	119.1 ± 23.3, 88.8 ± 50.4	12.4, 53.6, 34.0

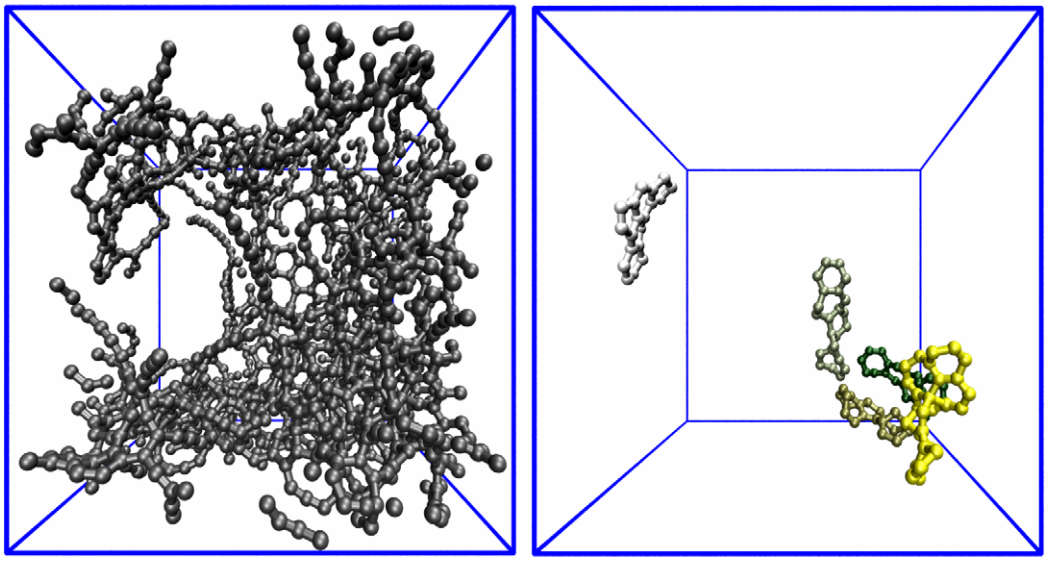

Fig. 2 – (Left) a molecular snapshot of the model for BPL illustrates the highly amorphous nature of the material. Spheres and cylinders are carbon atoms and carbon–carbon bonds, respectively. (Right) five representative graphene microcrystals identified in the BPL model using ring connectivity analysis. Their respective locations can be directly mapped onto the larger structure on the left by superimposing the unit cells.

number of carbon atoms in the system formed microcrystals showed that the microstructure was highly fragmented and that there was not a significant amount of ordering between carbon ring structures. The remaining carbon atoms that were not part of the microcrystals were found to be in ring structures and small chains that connected carbon rings and graphene sheets.

4.2. *Pore size distribution and specific surface area*

The PSD and SSA are among the most widely used properties to characterize the structure of porous materials, in part, because they can be estimated from adsorption isotherms and can be used to quantitatively compare different adsorbents. We calculated the total geometric PSD of the HRMC model. The comparison between the model PSDs and the QSDFT estimate of the PSD for BPL using experimental nitrogen adsorption data at 77 K are shown in Fig. 3.

In comparing the PSDs, it is important to note that the PSD obtained from the QSDFT analysis of experimental adsorption data is an estimate of the geometric PSD for BPL that is influenced by the specific nature of the adsorbate–adsorbate and adsorbate–adsorbent interactions, while the PSD for the model is simply based on the geometric considerations. Moreover, as He and Seaton [48] have recently demonstrated, estimates of the PSD obtained from the slit-pore interpretation of adsorption isotherms, for BPL in particular, vary widely depending on the details of the implementation. In order to provide a more direct comparison with the experimental estimate, we also used QSDFT to estimate the PSD of the HRMC model by analyzing simulated nitrogen adsorption data at 77 K (Fig. 4).

The experimental QSDFT estimate of the PSD for BPL had a wide range of pore sizes, with approximately 75% of the total pore volume distributed in pores less than 20 Å in diameter. The remaining fraction of the pore volume was a result of mesopores present in the sample. These regions of the PSD were not shown for the sake of clarity in comparing with the model's PSD. As evident from Fig. 3, both the geometric and QSDFT PSDs for the model structure were in very good agreement despite the underlying independent slit-pore assumption used in the QSDFT approach. Both PSDs for the model structure were much narrower than the experimental PSD, with a maximum pore size of only 12 Å. Thus, it was clear that the model did not accurately capture larger porous structures that are present in the real material. This discrepancy was a result of the fact that the RDF did not contain a sufficient amount of structural information to reconstruct these larger pores. This was consistent with the previous observation that the RDF determined from XRD contained almost no discernable features beyond 10 Å. This demonstrated

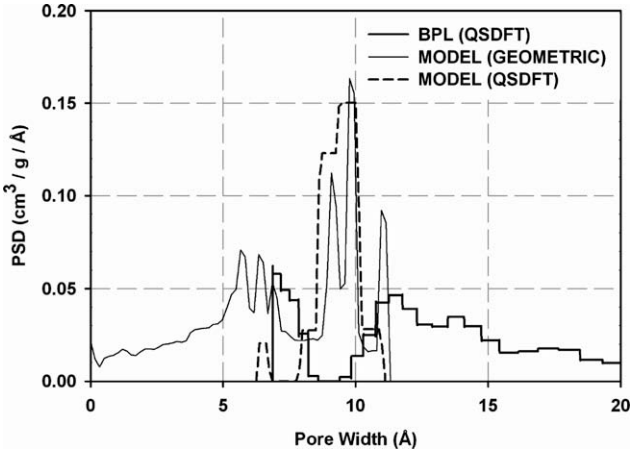

Fig. 3 – The pore size distribution for the BPL sample estimated using QSDFT and the geometric and QSDFT distributions for the HRMC-generated model. The geometric PSD shows small pores (< 2.5 Å) that are inaccessible to nearly all adsorbate molecules.

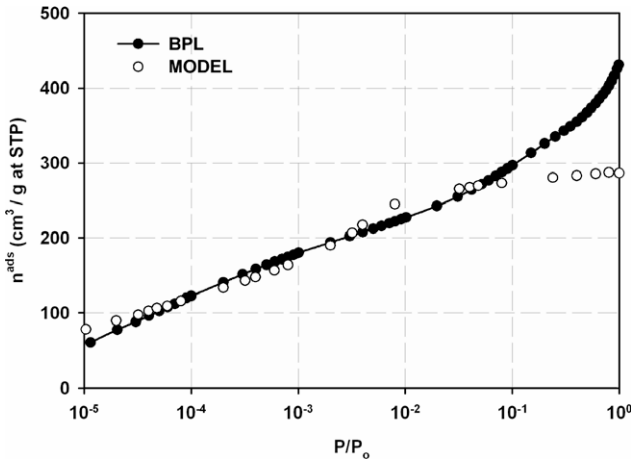

Fig. 4 – Simulated and experimental nitrogen adsorption isotherms for the HRMC model and the BPL sample, respectively.

a general limitation of the HRMC method that has not been previously addressed, namely that the RDF only describes fluctuations in the carbon density on short length scales and any reconstructive procedure solely based on this function will be unable to capture larger structural features. However, as we show in subsequent sections, the HRMC model was still able to accurately predict adsorption isotherms under the state conditions where small pores are the dominant structural features in determining the adsorptive properties of the material.

The SSA of the BPL sample and the model were also examined. The BET interpretation of the nitrogen adsorption data estimated the surface area for the BPL sample to be 1009 m^2/g, while the Connolly surface area for the model was 1027 m^2/g. The classical BET approach assumes that adsorbate molecules adsorb onto an energetically homogeneous surface. This is clearly not the case for highly heterogeneous materials such as microporous carbons. Coasne et al. [49] and Gelb and Gubbins [40] have shown that the agreement between the Connolly and BET surface areas is dependent on pore size, pore geometry and the characteristics of the adsorbate molecule. They showed that the two measures of surface area typically diverge for highly confined porous systems, due to energetic heterogeneities in the surface that arise from the curvature. Thus it is unlikely that the exceptional agreement between Connolly surface area for the HRMC model and the BET area for BPL can be generalized to other microporous systems.

4.3. *Adsorption equilibrium*

Although comparing structural features of the BPL sample and the model can be used to assess the validity of the model, it is essential to also compare the adsorptive properties in order to gain insight into the interplay between the structural and phenomenological properties. Using GCMC simulations and simple spherical Lennard-Jones representations for nitrogen, we calculated the nitrogen adsorption isotherm at 77 K for the model of BPL. The results from the simulations are compared with the experimental isotherm in Fig. 4.

As evident from Fig. 4, both the simulated and experimental isotherms appeared to be Type I isotherms as defined by the IUPAC classification system, and exhibited monotonic exponential curvature (linear on the log-scale of Fig. 4). This type of behavior is characteristic of predominately microporous materials and was consistent with the previous analysis of the PSDs. Both isotherms also showed that a significant amount of adsorption took place in the low pressure region, where $10^{-5} < P/P_o < 10^{-2}$. The micropores in the material provided a highly confined environment, in which the adsorbates' exposure to the carbon surface was maximized. Thus, adsorption into the micropores was most energetically favorable and dictated the features of the isotherms in the low pressure regime. In this region, the simulated and experimental isotherms were also in excellent agreement. However, for higher relative pressures, the simulated isotherm plateaued, while the adsorbed amount for the experimental isotherm continued to increase. The discrepancy at higher relative pressures occurs because only the microporosity of the BPL sample was captured in the model. Therefore the model reached a maximum in its adsorption capacity when the micropores became fully filled with nitrogen, while the experimental isotherm continued to increase because of the presence of mesopores, allowing for adsorption to continue once the micropores had reached their full capacity. This interpretation was consistent with the observation that the filling pressure for slit-pore widths corresponding to small mesopores occurs at $P/P_o \sim 10^{-2}$ [50].

We also used the model to study adsorption under high pressure conditions for carbon dioxide and methane. For comparison with experimental data, we turned to a previous experimental study by Reich et al. [51] in which they collected adsorption data for carbon dioxide and methane for bulk pressures up to 3.7 MPa. Isotherms were calculated for carbon dioxide and methane at 212.7 K, 260.2 K and 301.4 K. The results of these calculations and the experimental data from Reich et al. are presented in Figs. 5 and 6, for carbon dioxide and methane, respectively.

As was the case for nitrogen, the isotherms for carbon dioxide and methane appear to be Type I isotherms. For carbon dioxide the simulated isotherms slightly underestimated and overestimated the experimental results at low and high pressures, respectively. Since this trend occurred at all three temperatures, it indicated that both the interaction parameters for carbon dioxide–carbon dioxide and carbon dioxide–carbon may have needed additional modification to account for the anisotropic nature of the carbon dioxide. The HRMC model gave somewhat better results for the three methane adsorption isotherms. The predicted isotherms gave very good agreement at all three temperatures examined, with near perfect agreement in the low pressure regime of the isotherm.

To get a more detailed description of the adsorption energetics and potential effects of local chemical heterogeneities, we calculated the differential enthalpies of adsorption for the BPL sample and the HRMC model. The differential enthalpies of adsorption were calculated from the experimental isotherms using the following thermodynamic relationship,

$$q_d = -R\left(\frac{\partial \ln P}{\partial(1/T)}\right)\Big|_n, \tag{8}$$

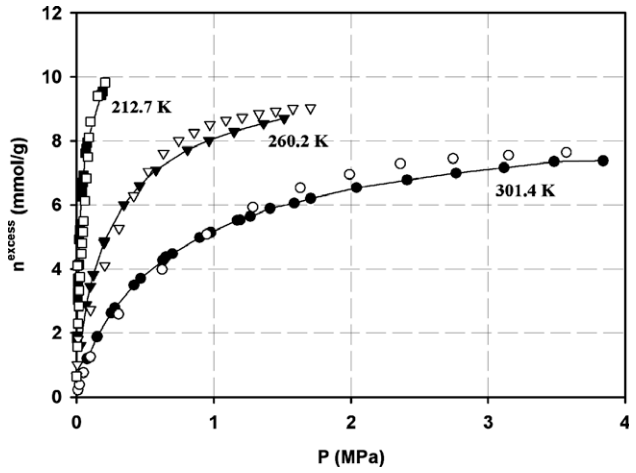

Fig. 5 – Carbon dioxide adsorption isotherms at 212.7 K (squares), 260.2 K (triangles) and 301.4 K (circles) for the BPL sample and the HRMC model. Filled symbols with lines are the experimental data taken from Reich et al. and unfilled symbols are predictions of the model.

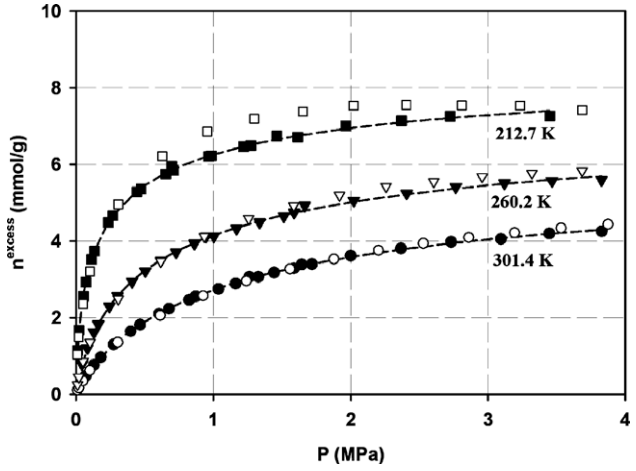

Fig. 6 – Methane adsorption isotherms at 212.7 K (squares), 260.2 K (triangles) and 301.4 K (circles) for the BPL sample and the HRMC model. Filled symbols are experimental data taken from Reich et al., dashed lines are Toth fits (see Eq. (9)) to the experimental data and unfilled symbols are predictions of the model.

where R is the gas constant. The derivative in Eq. (8) was evaluated by constructing a plot of $\ln P$ versus $1/T$. Linear regression was then used to estimate the slopes of the adsorption isosteres that were formed by connecting the points from the three isotherms at constant loadings. To obtain the points on the isotherms that corresponded to constant n, each of the three methane isotherms was fit to a Toth equation [36],

$$n = \frac{n_L P}{(b + P^m)^{1/m}}, \tag{9}$$

where P is the pressure and n_L, b and m are adjustable parameters. The Toth fits for the isotherms are shown in Fig. 6 alongside the experimental and simulated isotherms. These fits were used to find points at constant loading and calculate

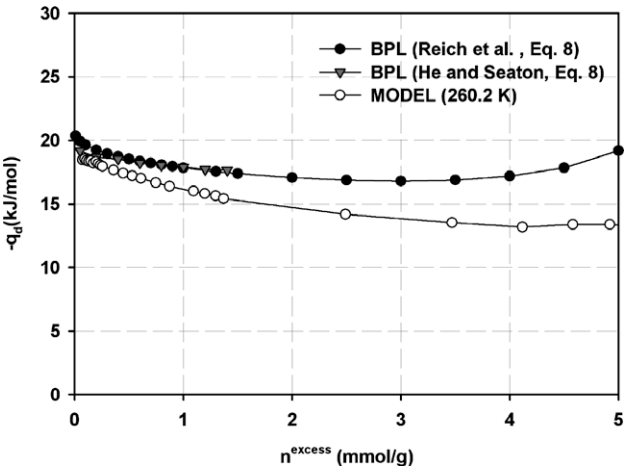

Fig. 7 – Differential enthalpies of adsorption for methane. Filled symbols are estimates from experimental measurements and unfilled symbols are predictions of the HRMC model.

the differential enthalpies of adsorption. The results for the BPL sample and the HRMC model are shown in Fig. 7.

In addition to comparing with the experimental estimates from Reich et al., we also show estimates of the differential enthalpies of adsorption taken from He and Seaton [48], which were obtained using a similar procedure.

The agreement between the experimental and model estimates of q_d was best in the low coverage, or low pressure region, where the methane–carbon interactions were dominant in determining adsorptive behavior. The under prediction of the model could have been attributed to error in estimating the carbon density and the scaling method used to determine the Lennard-Jones well-depth. It should be noted that the estimates made using Eq. (8) are least accurate in the low loading regime, due to the difficulty in accurately measuring the equilibrium pressure at these conditions. Both q_d plots were fairly flat, with no sharp decreases, which suggested that the energetic distribution of adsorption sites was fairly homogenous. However, there were significant discrepancies between the model and experimental results at higher loadings. This was due to the fact that at higher loadings the methane–methane interactions were the dominant contributions to q_d. The nature of these interactions is influenced heavily by pore size and pore morphology. In the case of the real material, once the micropores are completely layered with adsorbed methane, adsorption begins in the larger pores. At higher loadings, methane packs into these larger pores which are more energetically favorable than the layering that occurs under low loading conditions due to the relative strengths of the methane–methane and methane–carbon interactions. Consequently, the absence of these larger pores forces layering to occur at higher loadings and resulted in a decrease in simulated q_d.

5. Conclusions

We have presented a molecular model for BPL that was developed using the HRMC method. The model had a carbon density profile that was consistent with experimental XRD

measurements and a local bonding structure that was energetically stable. In addition, the model was able to capture many of the heterogeneous structural features of the real material, such as highly non-crystalline carbon ring structures, graphene fragments, pore connectivity and irregular pore morphologies. We demonstrated that the primary limitation of the model was its lack of large micropores and mesopores, which was a direct consequence of limited information contained within the experimental RDF. Nevertheless, we showed that the model could be used to accurately predict the adsorptive properties of the real material at low to moderate loadings for simple adsorbates such as nitrogen, carbon dioxide and methane. The lack of mesopores in the model did not have significant impact on the low pressure and low loading regions of the adsorption isotherms. It was only under higher pressures and higher loading conditions, where the micropores were filled, that major discrepancies between the experimental and simulated isotherms were observed. However, a study of the differential enthalpies of adsorption for methane provided a much more detailed description of the microstructure and the absence of mesopores was evident even under moderate loading conditions.

Acknowledgements

This work was supported by the US Defense Threat Reduction Agency (Project ID: AA07CBT011). We also acknowledge Prof. Teresa Bandosz (CUNY), Rick Beyer (US Army Research Laboratory) and Nathalie Cohaut (CRMD, Orléans) for their assistance in experimental data collection and analysis and for helpful discussions.

REFERENCES

[1] Kastening B, Heins M. Properties of electrolytes in the micropores of activated carbon. Electrochim Acta 2005;50(12):2487–98.
[2] Zhou Y, Wang Y, Chen H, Zhou L. Methane storage in wet activated carbon: studies on the charging/discharging process. Carbon 2005;43(9):2007–12.
[3] Zhu J, Figueiredo J, Faria J. Au/activated-carbon catalysts for selective oxidation of alcohols with molecular oxygen under atmospheric pressure: role of basicity. Catal Commun 2008;9(14):2395–7.
[4] Bansal R, Goyal M. Activated carbon adsorption. Boca Raton: CRC Press; 2005. p. 243–471.
[5] Bashkova S, Baker F, Wu X, Armstrong T, Schwartz V. Activated carbon catalyst for selective oxidation of hydrogen sulphide: on the influence of pore structure, surface characteristics, and catalytically-active nitrogen. Carbon 2007;45(6):1354–63.
[6] El-Sayed Y, Bandosz T. A study of acetaldehyde adsorption on activated carbons. J Colloid Interface Sci 2001;242(1):44–51.
[7] Przepiórski J, Yoshida S, Oya A. Structure of K_2Co_3-loaded activated carbon fiber and its deodorization ability against H_2S gas. Carbon 1999;37(12):1881–90.
[8] Bhattacharya S, Gubbins KE. Modeling triblock surfactant-templated mesostructured cellular foams. J Chem Phys 2005;123(13):1349071–7.
[9] Gelb L, Gubbins KE. Pore size distributions in porous glasses: a computer simulation study. Langmuir 1999;15(2):305–8.
[10] Kowalczyk P, Holyst R, Terzyk A, Gauden P. State of hydrogen in idealized carbon slitlike nanopores at 77 K. Langmuir 2006;22(5):1970–2.
[11] Lachet V, Boutin A, Tavitian B, Fuchs A. Molecular simulation of p-xylene and m-xylene adsorption in y zeolites. Single components and binary mixtures study. Langmuir 1999;15(25):8678–85.
[12] Do D, Do H. Evaluation of 1-site and 5-site models of methane on its adsorption on graphite and in graphitic slit pores. J Phys Chem B 2005;109(41):19288–95.
[13] Kanda H, Miyahara M. Freezing of Lennard-Jones fluid in cylindrical nanopores under tensile conditions. Adsorption 2007;13(3):191–5.
[14] Pikunic J, Clinard C, Cohaut N, Gubbins KE, Guet J, Pellenq R, et al. Structural modeling of porous carbons: constrained reverse Monte Carlo method. Langmuir 2003;19(20): 8565–82.
[15] Thomson K, Gubbins KE. Modeling structural morphology of microporous carbons by reverse Monte Carlo. Langmuir 2000;16(13):5761–73.
[16] Stuart S, Tutein A, Harrison J. A reactive potential for hydrocarbons with intermolecular interactions. J Chem Phys 2000;112(14):6472–86.
[17] van Duin A, Dasgupta S, Lorant F, Goddard W. ReaxFF: a reactive force field for hydrocarbons. J Phys Chem A 2001;105(41):9396–409.
[18] Opletal G, Petersen T, Malley B, Snook I, McCulloch D, Marks N, et al. Hybrid approach for generating realistic amorphous carbon structure using metropolis and reverse Monte Carlo. Mol Simulat 2002;28(10–11):927–38.
[19] Jain S, Pellenq R, Pikunic J, Gubbins KE. Molecular modeling of porous carbons using the hybrid reverse Monte Carlo method. Langmuir 2006;22(24):9942–8.
[20] Nguyen T, Cohaut N, Bae J, Bhatia S. New method for atomistic modeling of the microstructure of activated carbons using hybrid reverse Monte Carlo simulation. Langmuir 2008;24(15):7912–22.
[21] Palmer JC, Jain S, Gubbins KE, Fischer JE, Dash R, Gogotsi Y. Hybrid reverse Monte Carlo simulations of microporous carbons. Characterization of porous solids VIII. University of Edinburgh, Edinburgh, UK: RSC Publishing; 2008. p. 56–63.
[22] Bhattacharya S, Gubbins KE. Fast method for computing pore size distributions of model materials. Langmuir 2006;22(18):7726–31.
[23] Hassan N, Ghosh T, Hines A, Loyalka S. Adsorption of water vapor on BPL activated carbon. Carbon 1991;29(4–5): 681–3.
[24] Tsai W, Chang C. Adsorption of methylene chloride vapor on activated carbons. J Chem Technol Biotechnol 1994;61(2):145–51.
[25] Tsai W, Chang C. Surface characterization and thermodynamics of adsorption of methylene-chloride on activated carbons. J Environ Sci Health, Part A: Toxic/Hazard Subst Environ Eng 1995;30(3):525–35.
[26] Petit C, Karwacki C, Peterson G, Bandosz T. Interactions of ammonia with the surface of microporous carbon impregnated with transition metal chlorides. J Phys Chem C 2007;111(34):12705–14.
[27] Ding L, Bhatia S. Vacancy solution theory for binary adsorption equilibria in heterogeneous carbon. AIChE J 2002;48(9):1938–56.
[28] Jensen C, Seaton N, Gusev V, O'Brien J. Prediction of multicomponent adsorption equilibrium using a new model of adsorbed phase nonuniformity. Langmuir 1997;13(5):1205–10.
[29] Segarra E, Glandt E. Model microporous carbons: microstructure, surface polarity and gas adsorption. Chem Eng Sci 1994;49(17):2953–65.

[30] Liu J, Monson P. Molecular modeling of adsorption in activated carbon: comparison of Monte Carlo simulations with experiment. Adsorption 2005;11(1):5–13.
[31] Liu J, Monson P. Monte Carlo simulation study of water adsorption in activated carbon. Ind Eng Chem Res 2006;45(16):5649–56.
[32] Jain S, Gubbins KE. Ring connectivity: measuring network connectivity in network covalent solids. Langmuir 2007;23(3):1123–30.
[33] Franklin R. The interpretation of diffuse X-ray diagrams of carbon. Acta Crystallogr 1950;3(2):107–21.
[34] Soper A. Neutron scattering data analysis. In: Inst phys conf ser 107. Rutherford Appleton Laboratory, Chilton, UK: Institute of Physics Publishing; 1990. p. 57–67.
[35] Ravikovitch P, Neimark A. Density functional theory model of adsorption on amorphous and microporous silica materials. Langmuir 2006;22(26):11171–9.
[36] Rouquerol F, Rouquerol J, Sing K. Adsorption by powders & porous solids: principles, methodology and applications. London: Academic Press; 1999. p. 112.
[37] Nguyen T, Bhatia S, Jain S, Gubbins KE. Structure of saccharose-based carbon and transport of confined fluids: hybrid reverse Monte Carlo reconstruction and simulation studies. Mol Simulat 2006;32(7):567–77.
[38] Allen M, Tildesley D. Computer simulation of liquids. Oxford: Oxford University Press; 1989. p. 23–32.
[39] Franzblau D. Computation of ring statistics for network models of solids. Phys Rev B: Condens Matter Mater Phys 1991;44(10):4925–30.
[40] Gelb L, Gubbins KE. Characterization of porous glasses: simulation models, adsorption isotherms, and the Brunauer–Emmett–Teller analysis method. Langmuir 1998;14(8):2097–111.
[41] Frenkel D, Smit B. Understanding molecular simulation: from algorithms to applications. San Diego: Academic Press; 2002. p. 126–34.
[42] Steele W. The interaction of rare gas atoms with graphitized carbon black. J Phys Chem 1978;82(7):817–21.
[43] Klauda J, Jiang J, Sandler S. An ab initio study on the effect of carbon surface curvature and ring structure on $N_2(O_2)$-carbon intermolecular potentials. J Phys Chem B 2004;108(28):9842–51.
[44] Johnson J, Zollweg J, Gubbins KE. The Lennard-Jones equation of state revisited. Mol Phys 1993;78(3):591–618.
[45] Myers A, Monson P. Adsorption in porous materials at high pressure: theory and experiment. Langmuir 2002;18(26):10261–73.
[46] Vuong T, Monson P. Monte Carlo simulation studies of heats of adsorption in heterogeneous solids. Langmuir 1996;12(22):5425–32.
[47] Wyckoff R. Crystal structures. New York: John Wiley & Sons; 1963. p. 26.
[48] He Y, Seaton N. Monte Carlo simulation and pore-size distribution analysis of the isosteric heat of adsorption of methane in activated carbon. Langmuir 2005;21(18):8297–301.
[49] Coasne B, Gubbins KE, Pellenq R. A grand canonical Monte Carlo study of adsorption and capillary phenomena in nanopores of various morphologies and topologies: testing the BET and BJH characterization methods. Part Part Syst Char 2004;21(2):149–60.
[50] Lastoskie C, Gubbins KE, Quirke N. Pore size distribution analysis of microporous carbons: a density functional theory approach. J Phys Chem 1993;97(18): 4786–96.
[51] Reich R, Ziegler W, Rogers K. Adsorption of methane, ethane, and ethylene gases and their binary and ternary mixtures and carbon dioxide on activated carbon at 212–301 K and pressures to 35 atmospheres. Ind Eng Chem Proc DD 1980;19(3):336–44.